Inclusion of liquid crystalline azo-dyes in nanometric porous anodic aluminas: A comparative morphological and optical study

Omar G. Morales-Saavedra [a,*], Maria Esther Mata-Zamora [a], Ernesto Rivera [b], Tonatiuh García [b], J. Guadalupe Bañuelos [a], José M. Saniger-Blesa [a]

[a] *Centro de Ciencias Aplicadas y Desarrollo Tecnológico, Universidad Nacional Autónoma de México, CCADET − UNAM, Circuito Exterior Ciudad Universitaria, C.P. 04510, México D.F., Mexico*
[b] *Instituto de Investigaciones en Materiales, Universidad Nacional Autónoma de México, IIM − UNAM, Circuito Exterior Ciudad Universitaria, C.P. 04510, México D.F., Mexico*

Abstract

Prepared amorphous porous anodic alumina with average nanometric porous dimensions of 67 nm in diameter and 50 μm in depth was successfully used as host network for different liquid crystalline azobenzene compounds bearing oligo(ethylene glycol) segments. Since the implemented optical chromophores were specifically designed for quadratic non-linear optical applications, the obtained ordered hybrid structures were fully characterized according to the second harmonic generation technique following the Maker-Fringes method. Comparative linear optical absorption, Raman and X-ray photoelectron spectroscopic investigations were also carried out in order to evaluate the optical performance of these molecular systems within the 1D-nanotube-like confinement. Finally, atomic force microscopic studies of both the dissolved barrier layer and the porous cap were performed on the samples in order to explore surface morphology and assure best possible insertion of these azo-dyes within the pores of anodic alumina.
© 2007 Elsevier Ltd. All rights reserved.

Keywords: Porous anodic alumina; Azobenzene; Nanostructures; Non-linear optics; SHG

1. Introduction

Porous anodic alumina (PAA) has been known since the beginning of the 20th century for its high-tech importance in the industrial anodization of aluminum [1]. More recently, due to its ideal nanopore geometrical arrangement, it was proposed as a promising template for the growth of 1D ordered arrays such as bundles of nanotubes or nanowires [2−4], which constitute a critical step in the development of operative nanometric devices and prototypes. In fact, PAA templates with porous densities ranging from 10^9 to 10^{15} pores cm^{-2}, diameters (D) varying from 4 to 250 nm, typical tube lengths (L) ranging between 0.1 and 300 μm, and pore aspect ratios (L/D) from 10 to 1000 [5−8] are routinely prepared following well established fabrication techniques. In recent years a significant number of scientific papers have been published reporting the growth of carbon nanotubes [9−11], metallic nanowires, oxide and chalcogenide semiconductor nanowires [12−16], inside the porous PAA templates. In most of these works the PAA films are basically considered as mechanically inert supports, ready to be filled using a wide variety of techniques, such as the pyrolysis of hydrocarbon compounds, AC-electrochemical deposition or immersion in colloidal suspensions. These approaches work reasonably well in many cases, not taking into account, however, the specific chemical composition and properties of the nanopore walls which can play an important role in the definition of alternative synthetic routes for the preparation of a variety of new 1D nanostructures. In this sense, some authors have noted that the anodic alumina

nanopore walls seem to be active in processes such as the pyrolysis of hydrocarbons [17–19], ammonia sensing, and pyrene derivatives chemisorption layer onto porous alumina [20,21]. On the other hand, several works have been published concerning the physical and chemical characterizations, the composition and structure of anodic alumina [22–26]. Although most of that information is spread in different scientific reports, a considerably better understanding of the fundamental properties of these structures has already been achieved, giving rise to new and potential perspectives in emergent applied sciences such as opto-electronics and photonics, which are currently being considered as essential research fields for the development of advanced technological applications. Under this context, we present in this work a detailed optical and morphological comparative study of PAA prepared by the oxalic acid route [5,6], which has been filled with newly synthesized optical active liquid crystalline (LC) azobenzenes bearing oligo(ethylene glycol) segments (azo-dyes). These rod-like compounds have been specifically designed for quadratic $\chi^{(2)}$-non-linear optical (NLO) applications, such as optical second harmonic generation (SHG).

According to Rau, azobenzenes bearing both electron-donor and electron-acceptor groups belong to the "pseudostilbenes" category, where the $\pi-\pi^*$ and $n-\pi^*$ bands are practically superimposed but are actually inverted on the energy scale with respect to the non-substituted azobenzene bands [27]. Donor–acceptor substituted azobenzenes alone or incorporated into polymer systems provide very versatile materials from an applications point of view. It is well known that highly polar azobenzenes exhibit strong $\chi^{(2)}$-NLO properties such as SHG. Several azo-dyes and azo-polymers with potential NLO properties have been reported in the literature [28,29].

Previously, we reported the synthesis [30], optical properties and aggregation [31,32] of new amphiphilic liquid crystalline azo-dyes bearing end-capped oligo(ethylene glycol) segments: RED-PEGM-3, RED-PEGM-8 and RED-PEGM-10. The presence of an oligo(ethylene glycol) segment makes these molecules highly amphiphilic, without the necessity to introduce ionic groups, which is suitable for NLO LB applications [32]. According to the literature, azobenzene and poly(ethylene glycol) have been combined together in other systems such as copolymers [33,34], nanomaterials [35,36] and cyclodextrin polymers [37,38], in some cases forming supramolecular complexes with interesting properties [39].

The present paper provides experimental evidence concerning the possibility to create organic–inorganic 1D-NLO active hybrid structures implementing PAA templates and the newly functionalized LC azo-dyes. Recent investigations proved that organic materials represent a better alternative for NLO applications because of their ultrafast response times, lower dielectric constants, better processability characteristics and enhanced NLO responses [40–46]. It is well known that second order NLO materials must contain second harmonic chromophores, which have to be arranged macroscopically in a non-centrosymmetric manner. Such highly ordered arrangements can be achieved by self-assembly techniques, electrical poling by high voltage DC fields or building Langmuir–Blodgett films in the case of amphiphilic molecules [40–49]. Azo-dyes and azo-polymers have been widely studied by many research groups due to their versatility in the domain of optics, NLO and photonics applications implementing the previously mentioned assembling methodologies. In the current case, experimental results indicate that the PAA templates can also provide an optional induced ordered 1D-array, which supports the organic chromophores giving rise to measurable NLO effects including SHG. The comparative morphological, spectroscopic and optical studies presented in this report can be useful for future modification of the chemical functionality of both the porous anodic aluminas and the azobenzene based NLO chromophores.

2. Experimental section

2.1. NLO azo-dyes

As shown in Fig. 1, three novel LC azo-dyes were implanted within the 1D nanotubes of PAA templates: (a) [1-*N,N*-dimethylamine-4'-nitroazobenzene] named here RED-Me, where $R_1 = R_2 = CH_3$, (b) [*N*-methyl-*N*-{4-[(*E*)-(4-nitrophenyl)diazenyl]phenyl}-*N*-(3,6,9,12,15,18,21-heptaoxadeutaeicos-1-yl)-amine], named here RED-PEGM-7, where $R_1 = CH_3$ and $R_2 = (CH_2CH_2O)_7CH_3$), and finally (c) [*N*-{4-[(*E*)-(4-nitrophenyl)diazenyl]phenyl}-*N,N*-di(3,6,9,12,15,18,21-heptaoxadeutaeicos-1-yl)amine], named here: RED-DIPEGM, where $R_1 = R_2 = (CH_2CH_2O)_7CH_3$. The synthetic route employed to obtain RED-PEGM-7 is similar to that used to synthesize the RED-PEGM-*n* (*n* = 3, 8, 10) compounds [30]. Compounds RED-PEGM-7 and RED-Me show a powder-like structure at room temperature, whereas RED-DIPEGM exhibits a viscous LC state. The corresponding dipole moments were calculated
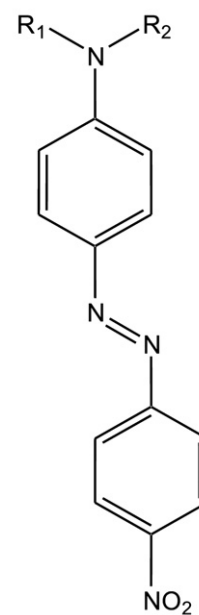

Fig. 1. Molecular structures for RED-Me ($R_1 = R_2 = CH_3$), RED-PEGM-7 ($R_1 = CH_3$, $R_2 = (CH_2CH_2O)_7CH_3$), and RED-DIPEGM ($R_1 = R_2 = (CH_2CH_2O)_7CH_3$).

by semi-empirical methods (AM1 and PM3), giving high dipole moment values ranging from 9 to 11 D as shown in Table 1.

2.2. Porous anodic alumina template preparation and insertion of LC azobenzenes

High purity aluminum (99.999%) foils with a thickness of 0.13 mm were used as starting material. Prior to anodization, aluminum was annealed under air at 480 °C for 1 h. The annealed plates of 10×25 mm were electrochemically polished (1:5 v/v of EtOH/HClO$_4$), and then mounted as the anode in an electrochemical cell using a graphite cathode. The preparation of oxalic porous anodic aluminas was carried out using standard conditions widely reported in the literature [5,6,22,26], where 0.3 M of oxalic acid at 40 V was used to induce anodization of Al. The temperature bath was kept at 10 °C and the anodization time was fixed to 8 h in order to obtain film thickness of about 50 µm. Aluminum was then electrochemically removed (electrochemical etching in 20 wt% HCl solution, with an operating voltage in the range of 1−5 V) in a circular defined area using elastic O-rings, leaving freestanding alumina windows in mechanically stabilizing Al frames [50]. Thus, porous anodic alumina templates conformed by hexagonal pore arrays with a 138 nm interpore distances formed by self-organization in the anodic alumina are obtained [5]. The circular working surface size was in the order of 7−8 mm in diameter. Afterwards, an etching chemical attack via phosphoric acid (0.5 M at 35 °C for 35 min) was carried out in order to fully open the nanopores of the anodic alumina, producing the 1D-nanotube-like array [51]. This etching process also leads to some pore widening so that the observed pore diameters do not reflect the intrinsic properties of the anodization process. By this methodology, 1D nanotubes varying in the range of 44−67 nm in diameter were obtained for the opened barrier layer and the porous cap. Both surfaces were carefully monitored by AFM in order to assure optimal widening.

Once the 1D nanotube anodic alumina membranes (AAMs) were optimally produced, 6 mg of LC-RED-PEGM-7 and RED-Me azo-dyes was fully dissolved in 5 ml of tetrahydrofuran (THF) in order to obtain saturated dissolutions; the RED-DIPEGM sample was used in its natural LC state to fill up the 1D-nanotube arrays. AAMs were mounted with the porous cap placed upwards onto the input tap of a low power vacuum system (Air CADET, vacuum/pressure station, ColPalmer). In order to avoid any damage to the fragile AAO-membrane due to excessive low pressure, the membranes were supported by a thin metallic rigid grid. Afterwards, by using a micropipette, the rounded AAMs were fully covered with the LC azo-dye dissolutions (using consistently the same amount in volume:

0.4 ml); the vacuum system was then started at 50 kPa and the inclusion of the NLO molecules within the 1D-AAM nanotubes was mechanically induced. Subsequently, both the porous and the opened barrier layers of AAMs were carefully cleaned with THF-damped optical tissues in order to remove any dissolution overload. The hybrid samples were isolated while drying with a plastic cover in order to avoid atmosphere and temperature variations, and conserved for 1−2 weeks at room conditions in closed recipients with a small hole in the cap in a clean-dry-dark environment. Pure AAMs were also prepared for reference and calibration purposes.

2.3. Physical characterization techniques

Standard physical characterization techniques were applied to pure reference AAM and to the AAM-hybrid composites in order to determine their structural and physical properties: (i) the morphology of the films was studied by atomic force microscopy (AFM) (Park AutoProbe CP equipment), where the acquisition of images was performed in contact mode with an interaction force applied between the sample and the AFM-tip of 1.5 nN. The AFM system was equipped with a SiN sharpened Microlever™ tip with typical force constant of 0.05 N m^{-1} and resonant frequency of 22 kHz which specify the mechanical characteristics of the used cantilever (typical constants of the instrument). Both the porous cap and the barrier layer were carefully monitored by AFM in order to assure optimal quality of AAM and the insertion of guest molecules. (ii) Linear optical absorption spectra were obtained in the 200−1100 nm range using a double beam Shimadzu UV−vis spectrophotometer, taking air in the reference beam. (iii) An Almega XR Dispersive Raman spectrometer equipped with an Olympus microscope (BX51) was used to obtain the Raman spectra of the samples. An Olympus 50× objective (N.A. = 0.45) was used as focusing optical system for the Raman laser source (see below); the spot size of the focused laser beam on the sample was ∼1.5 µm^2. The same objective was also implemented as collecting optical system for the back-scattered light in a 180° backscattering configuration. The scattered light was detected by a charge coupled device (CCD) detector, thermoelectrically cooled to −50 °C. The spectrometer used a convenient optical grating (675 lines mm^{-1}) to resolve the scattered radiation and a notch filter to block the Rayleigh light. The pinhole of the monochromator was set at 25 µm and the Raman spectra were integrated over 20 s with a resolution of ∼4 cm^{-1}. The excitation source was obtained from a Nd:YVO$_4$ laser (frequency doubled at 532 nm) and the incident power at the sample was of ∼8 mW. (iv) X-ray photoelectron spectroscopy (XPS) was carried out in order to provide any evidence of chemical binding between the AAM surface and the implemented LC azo-dyes. To this end, a monochromatised Al Kα ($h\nu$ = 1486.6 eV) X-ray generator source and a system of ultra high vacuum VG-Scientific Microtech Multilab ESCA2000 were used with a CLAM4 hemispheric electron spectrometer. The XPS were obtained at a take-off angle of 55° with respect

Table 1
Dipole moments of the azo-dyes calculated by semi-empirical (AM1 and PM3) methods

Azo-dye	AM1 (D)	PM3 (D)
RED-Me	9.40	9.02
RED-PEGM-7	10.2	8.16
RED-DIPEGM	11.32	8.29

to the surface of the sample. The XPS polymer technique is discussed in detail and described by *Beamson and Briggs* [52]. For reference purposes, the binding energy peak of the Au $4f^{7/2}$ orbital positioned at 84.00 eV was used. The spectrometer calibration was performed with the Ag $4d^{5/2}$ (368.21 eV) line (resolution of the FWHM of 1.00 eV). The chamber pressure was kept constant during XPS measurements at 5×10^{-9} mb. The surface of the films was etched during 2 min with 3.0 kV Ar^+ at 0.024 $\mu A/mm^2$. Finally, the analysis of the spectra was performed by means of the SDPv4.1® software [53]. (v) The hybrid AAM composites were studied as active media for quadratic $\chi^{(2)}$-non-linear optical effects such as SHG. The SHG experimental device is shown schematically in Fig. 2: a commercial Q-switched Nd:YAG Laser system (Surelite II from Continuum, $\lambda_\omega = 1064$ nm, repetition rate of 10 Hz and a pulse width of $\tau = 12$ ns) was implemented to provide the fundamental wave. Typical pulse powers of 100 μJ were filtered in order to irradiate the samples by means of a $f = 50$ mm focusing lens, thus peak irradiances in the order of 20 MW cm^{-2} were achieved at the focal spot on the AAM-hybrid composites. This value was slightly below the energy damage threshold supported by the samples under strong focused beam irradiation. The polarization of the fundamental beam (S or P polarizing geometry) was selected by means of an IR-coated Glan-Laser polarizer and a $\lambda/2$-Quarz-retarder. A second polarizer was used as analyzer allowing the characterization of the SHG signals. The second harmonic waves (at $\lambda_{2\omega} = 532$ nm) were detected by a sensitive photomultiplier tube (HAMAMATSU R-928) behind interferential optical filters (centered at 532 ± 5 nm). The SHG device was calibrated by means of a Y-cut α-quartz crystal, wedged in the d_{11}-direction ($d_{11} = 0.64$ pm/V), which is commonly used as an NLO-reference standard via the *Maker*-Fringes method [41,44–46,54].

3. Results and discussion

3.1. Morphological AFM studies

The morphological structure of developed reference AAM is shown in Fig. 3. The AFM micrographs demonstrate in fact that the undoped nanotube arrays obtained for the oxalic anodic

alumina template exhibit average diameters varying from 44 to 67 nm. Fig. 3a and b corresponds to a typical porous cap and opened barrier layer, respectively. In both cases well defined geometrical patterns can be observed, where hexagonal structures forming ordered 2D-arrays can be easily recognized. The opened barrier layer illustrates slightly smaller porous dimensions; this is understandable because after the anodization process, the applied chemical attack selectively operates at different depths within the forming 1D-nanopore walls. In fact porous anodic films contain significant amounts of acid anions incorporated from the anodizing electrolyte and the distribution of electrolyte anions across the cell material is not uniform. A region of Al oxide extending from the pore wall contains relatively large acid anion content. At the same time an inner region of oxide is relatively pure Al oxide [22–26]. All this means that the upper walls of the nanopores present drastic physical and chemical structural changes, compared to that suffered by the lower ones, which allow a faster degradation produced by the phosphoric acid. In the case of non-optimal chemical attack and anodizing conditions, the barrier layer cannot be completely widened; consequently, fully capped nanopore structures are obtained as is shown in Fig. 3c.

Once the higher quality AAMs have been selected, the insertion of LC azo-dyes was properly carried out. Fig. 4 shows AFM micrographs (1×1 μm resolution) of: (a) RED-Me, (b) RED-PEGM-7 and (c) RED-DIPEGM based AAM-hybrid composites. It is observed from these images that all molecular structures were successfully embedded within the AAM nanotubes, as the nanopore arrays appear at least partially filled in all cases. In fact, there is no clear and definitive difference between the AFM micrographs shown in Fig. 4a–c for the hybrid structures; hence it is very difficult to estimate from these AFM micrographs the material penetration inside AAM in order to quantitatively evaluate the best molecular insertion. Since it is not possible to accurately evaluate the material penetration inside AAM by the available experimental techniques, we can only argue that only a moderate, but non-negligible material penetration inside AAM was achieved for the implemented molecular structures. Last asseveration, as will be shown later in Section 3.3, is supported by several Raman and SHG studies which demonstrate an important molecular insertion within AAM.
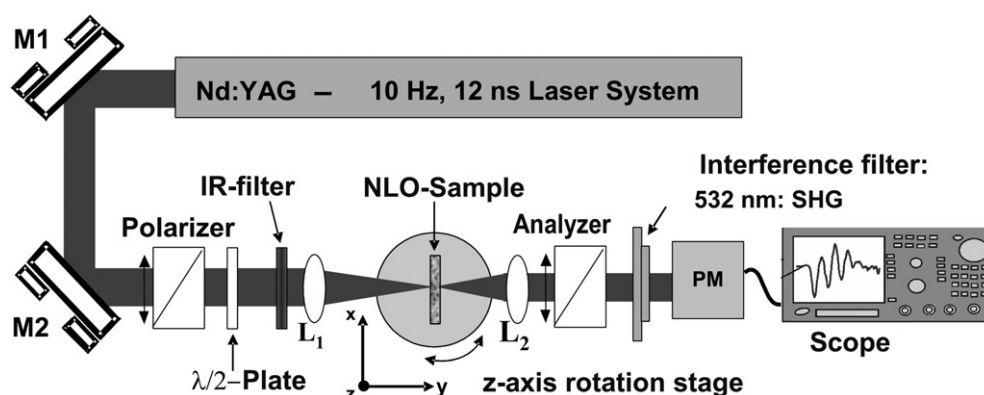

Fig. 2. Experimental set-up for SHG measurements in AAM-hybrid composites.
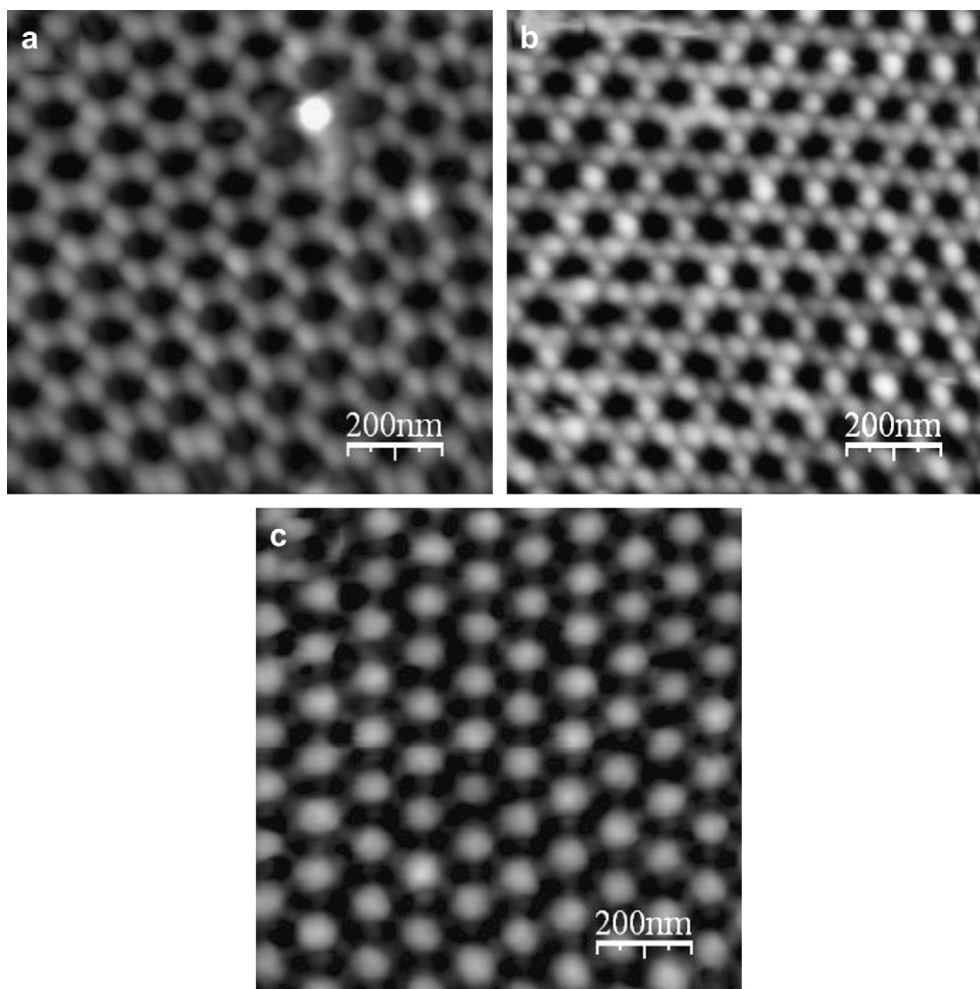
Fig. 3. AFM micrographs of oxalic AAM: (a) the porous cap, (b) the opened barrier layer, and (c) a closed barrier layer.

The observed moderate inclusion of the NLO compounds occurs, in principle, due to vaporization of the solvent used (THF) for RED-PEGM-7 and RED-Me compounds, while the intrinsic viscosity of RED-DIPEGM, contrary to expectations, restrains the inclusion of this compound within the AAM nanotubes. According to several experiments, it is concluded that optimal THF/azo-dyes' dissolution ratios should be achieved in order to regulate the viscosity and concentration of the dopant dissolutions, obtaining consequently best possible conditions for the insertion of azo-dyes inside the nanometric pores according to the implemented mechanically induced insertion method. On the other hand, a more detailed inspection of the micrographs displayed in Fig. 4 shows that the guest molecules tend to aggregate on the walls of the nanotubes in order to find mechanical support after drying (in the case of the dissolved molecules). The same effect occurs for LC-RED-DIPEGM compound. Chemical interactions between LC azo-dyes and the AAM nanotubes are also possible as it is discussed in next section. Compound RED-Me was easily removed from AAM by washing the sample with different solvents (THF and toluene); this fact demonstrates a weak mechanical interaction between this azo-dye and AAM. However, compounds RED-PEGM-7 and RED-DIPEGM

were not easily removed from AAM; even after dipping the respective hybrids for several days in these solvents, an important part of these molecules remained inside AAM (absorption spectra not shown here). The RED-PEGM-7 based hybrid offered major resistance to be removed from the AAM nanotubes by washing. These observations strongly suggest chemical interactions of these azo-dyes with AAM, including possible atomic binding as it is discussed in next section.

3.2. XPS measurements

XPS studies were carried out in order to provide any evidence of chemical binding between the AAM surface and the implemented LC azo-dyes. The survey spectra after calibration in C 1s (284.5 eV) and the high resolution XPS signals determined the chemical states of the studied samples. The obtained position core level for Al_2O_3 crystalline (sapphire reference) peaks of O 1s (BE = 530.87 eV) and Al 2p (BE = 64.5 eV) was clearly identified (see Fig. 5a and b). On the other hand, the substrate of AAM corresponds to Al 2p (BE = 63.30 eV, see Fig. 5b) and O 1s (BE = 531.49 eV). For the RED-Me hybrid sample, the respective related signals are located at BE = 63.35 eV and BE = 531.43 eV; for the
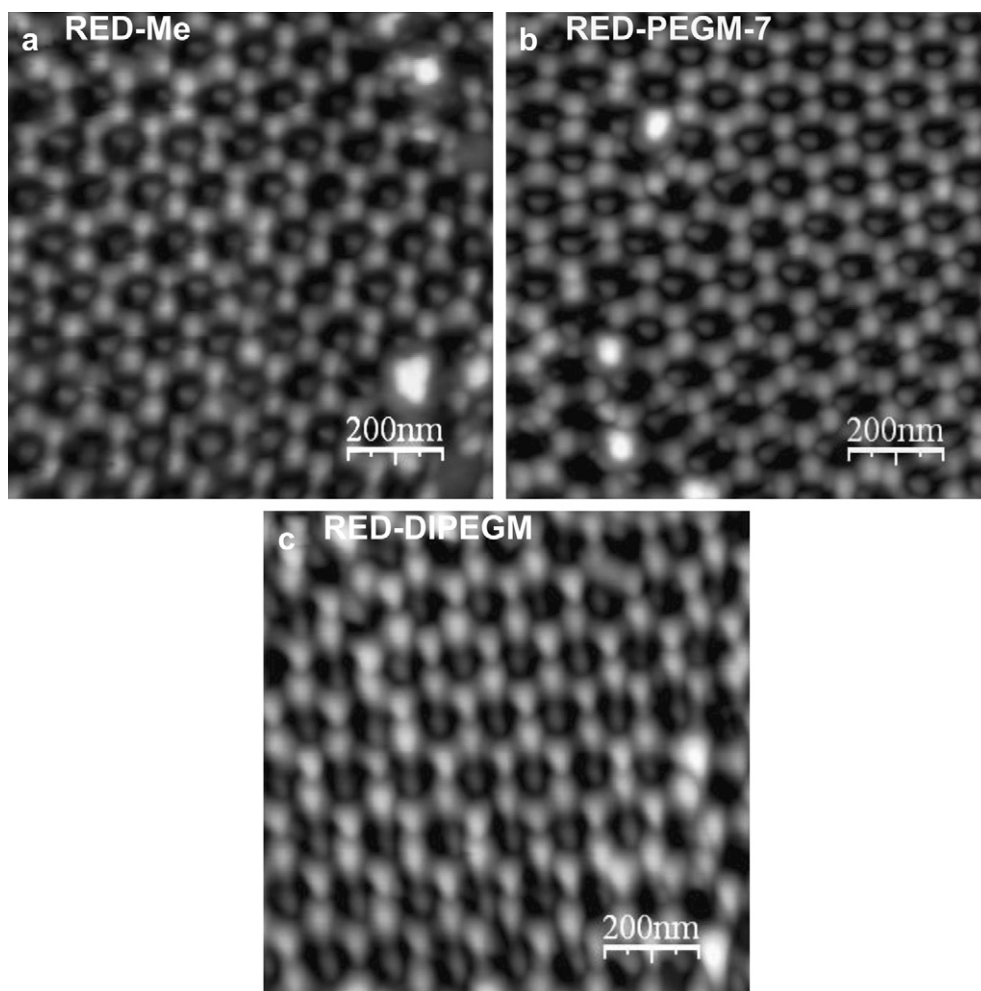
Fig. 4. AFM porous cap micrographs of LC-azobenzene based AAM-hybrid composites: (a) RED-Me hybrid, (b) RED-PEGM-7 hybrid, and (c) RED-DIPEGM hybrid.

RED-PEGM-7 hybrid sample these signals correspond to 64.10 and 531.44 eV; and finally for the REG-DIPEGM hybrid sample we have 63.65 and 531.43 eV, respectively. The position core level of C 1s does not modify the positions and symmetry in the high resolution XPS peaks.

As explained, a clear difference between the O 1s orbitals of the Al_2O_3 crystalline reference and AAM can be observed (see Fig. 5a); this chemical shift is produced by the respective modification of the material networks and a surface oxygen increase content over all the AAM nanotubes. A comparative and careful convolution analysis of the XPS of the hybrid samples in relation to the pure AAM-nanotube arrays provides important information concerning the chemical interaction of the embedded guest molecules with the host AAM. In fact, the differences observed in the positions of the Al 2p and O 1s orbitals for the different hybrids allowed us to provide some interesting insights of AAM/LC azo-dyes interactions: (1) by introducing LC azo-dyes within the AAM nanotubes, the oxygen atoms are displaced and a notable interaction in the Al 2p orbital is produced. This effect produces Al 2p BE-orbital shifts in the order of BE = 0.08, 0.90 and 0.35 eV for the RED-Me, RED-PEGM-7 and RED-DIPEGM

molecules, respectively; the O 1s chemical shift is in all cases negligible. (2) Last results are very significant since the maximal chemical shift corresponds to RED-PEGM-7 compound, indicating that this azo-dye strongly interacts with the Al atoms of the AAM nanotubes. In fact, as explained in the last section, the RED-PEGM-7 based hybrid showed the highest stability and the guest compounds cannot be easily washed out by using different solvents. It is well known that anodic porous alumina exhibits electro-catalytic activity; thus it is possible that the AAM nanotubes may act as nanoreactors where ionic interactions occur (probably Van der Walls and/or H-bridge bonding between the polar RED-PEGM-7 compound and the AAM nanowalls). (3) Surprisingly, the chemical shift for the REG-DIPEGM based hybrid is smaller (BE shift of the Al 2p orbital of 0.35 eV), although the presence of two oligo(ethylene glycol) segments in the molecular structure enhances its charge transfer character (see next section). Probably the lower chemical interaction of this compound with AAM is related to the stronger tendency of this molecule to form molecular aggregates compared to its RED-PEGM-7 analogue (see next section). Besides, this compound was introduced in its natural LC state (not dissolved in THF) at
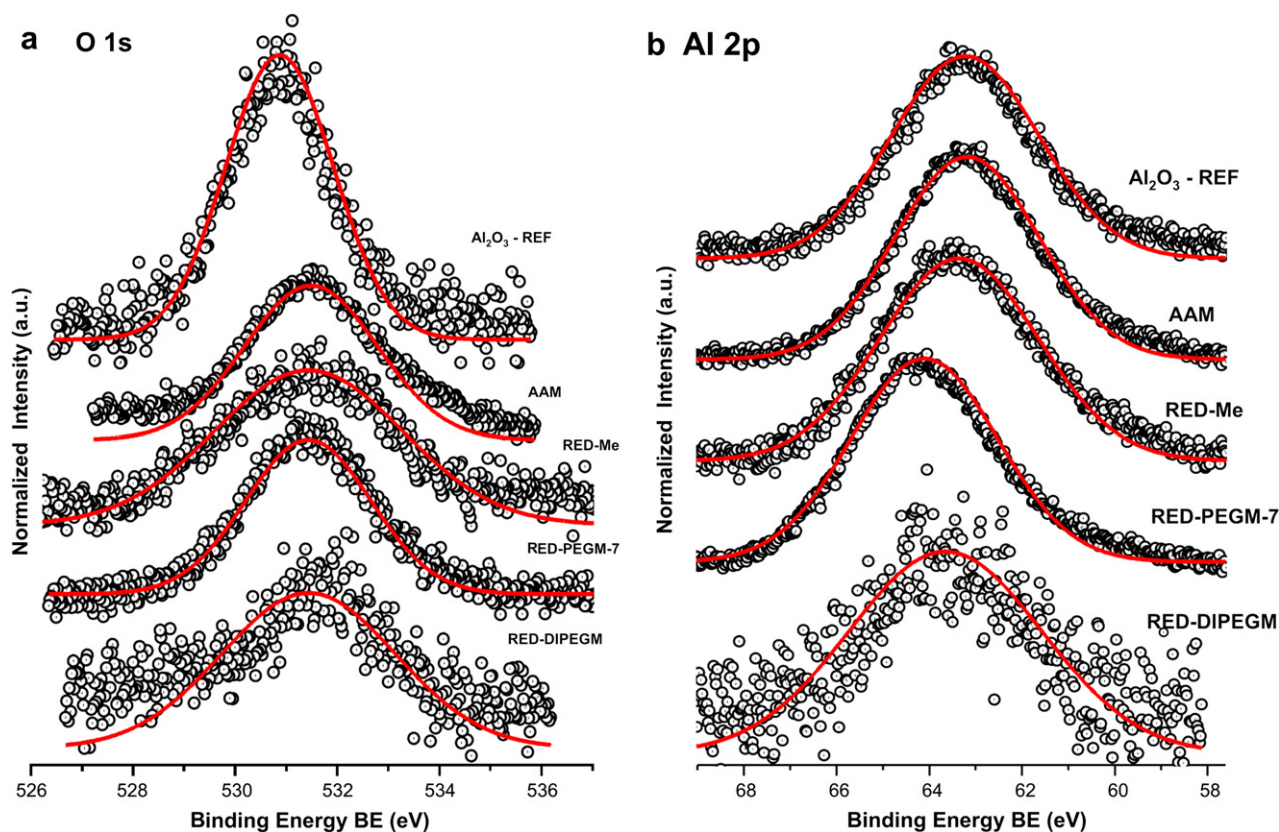
Fig. 5. High resolution XPS core level measurements: (a) O 1s and (b) Al 2p.

room temperature inside AAM. (4) Finally, the RED-Me based hybrid shows the lowest chemical interaction with AAM as the BE shift of the Al 2p orbital is extremely small. In fact, due to the lower polarity of this compound, rather rare possibilities of atomic binding may occur due to electronic interaction (charge transfer) of AAM with this compound. In this case, the small BE shift may be more related to a distortion of the BE caused by electronic repulsion between the Al atoms of the AAM nanotube surfaces and this molecular structure. In fact and consistent with the previous section, this compound was easily removed from AAM by washing the samples with different solvents; only a weak mechanical interaction (adhering effect) between this partially polar azo-dye and AAM tends to occur.

3.3. Linear and non-linear optical properties

In addition to the AFM/morphological and XPS characterizations, comparative optical studies such as UV–vis linear absorption and Raman spectroscopies were implemented in order to verify the insertion of the NLO molecules inside the porous anodic alumina and the optical performance of the hybrids. In fact, the hybrid AAM:azo-dyes were obtained from saturated THF dissolutions in order to achieve highest possible molecular loading inside AAMs; hence the absorption intensity of these hybrids is too strong to know details about the absorption bands of the molecular structures. For this

reason, in Fig. 6a, the absorption spectra obtained from non-saturated THF solutions are presented (mass compound: 0.072 mg, THF solvent: 4 ml).

Aminonitro substituted azobenzenes belong to the third category of the Rau classification; the $\pi-\pi^*$ and $n-\pi^*$ bands are inverted in the scale of energy and are totally superimposed [29]. According to Fig. 6a, the absorption spectrum of RED-Me in THF solution shows a well defined band at 474 nm due to the $\pi-\pi^*$ and $n-\pi^*$ transitions. Similarly, RED-PEGM-7 in THF solution exhibits an absorption band at 483 nm, 9 nm red shifted compared to that of RED-Me. This is an indication that this dye possesses a higher charge transfer character due to the presence of the oligo(ethylene glycol) segment [30]. In a previous work, we proved the formation of an intramolecular charge transfer complex in this molecule due to the coiling of the oligo(ethylene glycol) segment around the azobenzene unit [31,32]. On the other hand, the absorption spectrum of RED-DIPEGM in THF solution shows a maximum absorption wavelength at 445 nm, 29 nm blue shifted compared to that of RED-Me, preceded by a shoulder at 369 nm, which indicates the presence of H-aggregates for this dye. According to the absorption spectrum it seems that RED-DIPEGM forms aggregates more easily than its analogues RED-Me and RED-PEGM-7. Besides, the presence of two oligo(ethylene glycol) segments in the molecule enhances its charge transfer character and makes it more sensitive to the polarity of the solvent. These observations match
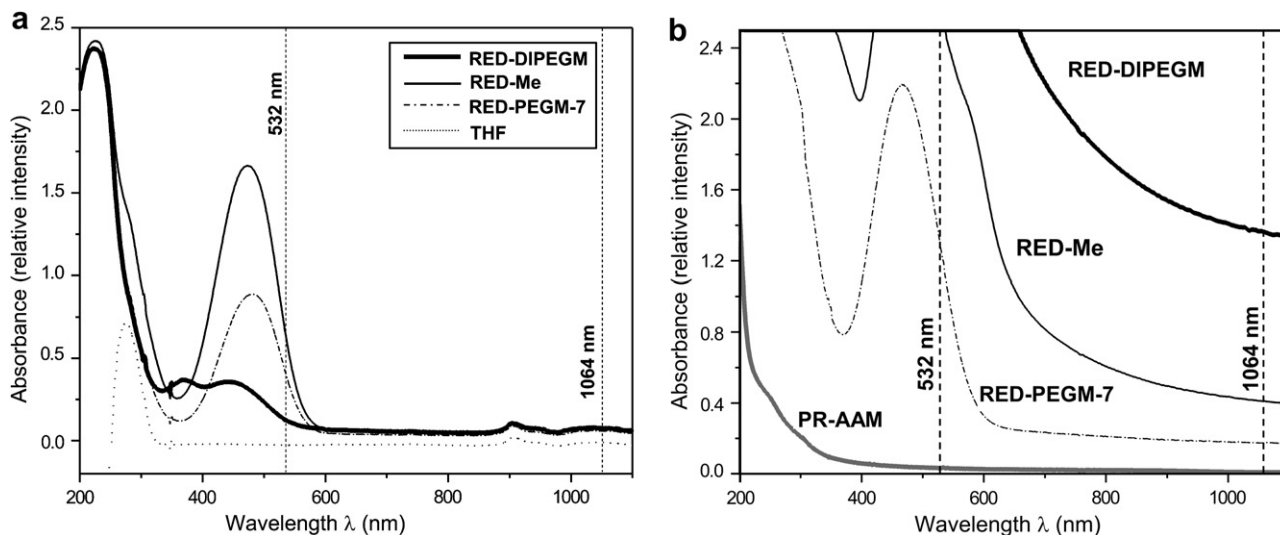
Fig. 6. (a) Comparative absorption spectra of the RED-Me, RED-PEGM-7, and RED-DIPEGM LC molecular systems in non-saturated THF solutions and (b) comparative absorption spectra of the PR-AAM and the RED-Me, RED-PEGM-7, and RED-DIPEGM based hybrid composites.

well with the dipole moments listed in Table 1. According to these results the charge transfer character in decreasing order is RED-DIPEGM > RED-PEGM-7 > RED-Me.

Fig. 6b shows the optical absorption spectra of both a pure AAM reference (PR-AAM) and the hybrid composites. It is observed that the PR-AAM is nearly transparent within the vis−NIR region, showing higher absorption to the UV which reveals suitable conditions for optical applications. In general, the RED-Me and RED-DIPEGM based hybrids exhibit saturated absorption bands in the ranges of 200−550 and 200−700 nm, respectively. The RED-Me hybrid reveals a weak optical window in the violet−blue region from 350 to 420 nm only. Finally, the RED-PEGM-7 composite exhibits saturated absorption from 200 to 370 nm, a lower absorption band in the range of 370−550 nm and negligible absorption from 570 to 1100 nm. Particularly, the RED-Me and RED-DI-PEGM based hybrids exhibit saturated absorption bands around 440 nm. RED-DIPEGM exhibited a tail at 650 nm whereas RED-Me exhibited a shoulder at 600 nm, which clearly indicates the presence of J-aggregates for these dyes in the network [31]. On the other hand, the RED-PEGM-7 composite exhibits a maximum absorption wavelength at 430 nm, the presence of aggregation is possible but it is not evident.

If we compare the absorption spectra of the dyes in solution and in the networks, we can observe a significant blue shift in the azo-dye based hybrids compared to the respective solutions. For instance, RED-PEGM-7 exhibits a $\lambda_{\max} = 483$ nm in solution, whereas in the based hybrid this band appears at $\lambda_{\max} = 430$ nm (53 nm blue shifted). This blue shift is an indication of a lowered charge transfer character in this environment; however, since the concentration of the doping dyes increases, this favors the aggregation phenomena of the azo-dye molecules inside the nanotubes.

Although RED-DIPEGM possesses a higher dipole moment (see Table 1), the optical performance of RED-PEGM-7 makes this compound a better candidate for the observation of $\chi^{(2)}$-NLO effects such as SHG by working with the standard

fundamental wavelength of a YAG-Laser system ($\lambda_\omega = 1064$ nm). In such case, the NLO-frequency doubled beam (at $\lambda_{2\omega} = 532$ nm) would not be drastically self-absorbed by the NLO chromophores, allowing at least near-resonant experimental conditions.

On the other hand, since usual aggressive chemical attack methodologies cannot be applied to our fragile organic based composites in order to detach the nanostructures from AAM for transmission electron microscopic (TEM) observation [55,56], we therefore performed Raman spectroscopic studies on the three pristine molecular systems and to their respective hybrid structured composites under different optical excitation geometries: (a) straight irradiation onto the porous cap and opened barrier layers and (b) optical excitation inside the host nanotubes. This latter measurement was achieved by cautiously cutting the hybrid porous membrane and micromechanically focusing the laser beam of the Raman system into the exposed nanotube cross-sections. Since AAM film thickness is in the order of 50 μm and the laser spot is ∼1.5 μm², optimal laser excitation of the exposed nanotubes can be easily achieved by this method. Fig. 7 shows the Raman signals obtained under such experimental geometries; here, the characteristic Raman peaks obtained from the pristine, non-confined compounds (black lines in Fig. 7b−d) and the Raman signals obtained from the pure AAM reference sample (Fig. 7a) are compared to that measured for the hybrid structures under such experimental conditions, as explained below.

In Fig. 7a, the Raman-fluorescence signals obtained from the reference PR-AAM for the three experimental geometries are displayed; it is noted that strongest fluorescence emission appears when laser excitation is carried out within the nanotube walls (green line), whereas considerable lower intensity emissions are observed from the porous cap layer (PCL: red line) and the opened barrier layers (OBLs: blue line). This is due to the larger effective excitation area achieved within the continuous nanotube cross-sections. Emissions of the PR-AAM exhibit an increasing linear, monotonic dependence
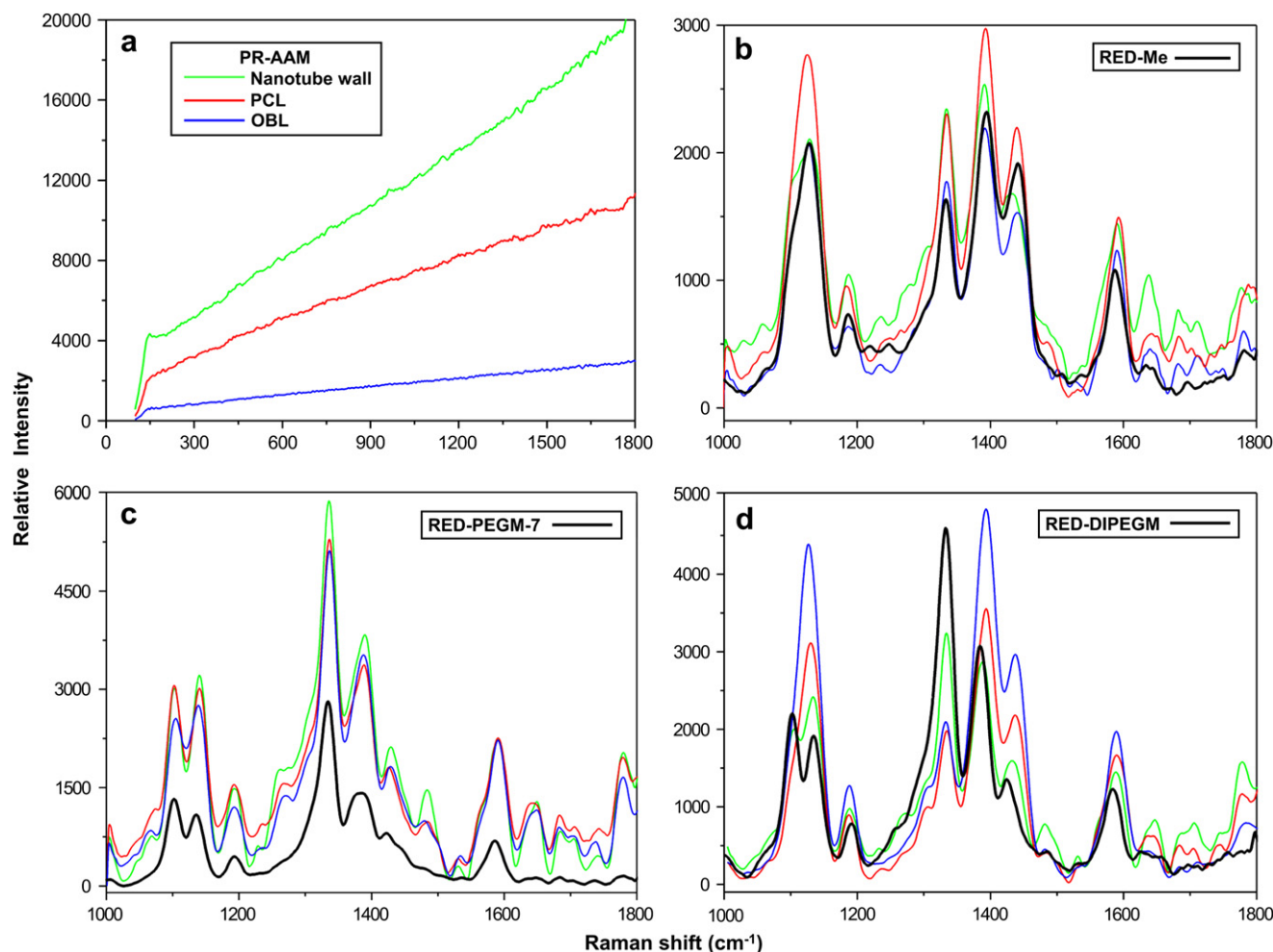
Fig. 7. Comparative Raman/fluorescence spectra of: (a) PR-AAM sample, (b) RED-Me, (c) RED-PEGM-7, and (d) RED-DIPEGM based composites. Measurements were performed under different optical excitation geometries: inside the nanotube cross-section (green lines), on the opened barrier layer (OBL: blue lines), on the porous cap layer (PCL: red lines) and finally, on a pristine, non-confined LC azo-dye sample (black lines). (For interpretation of the references to color in this figure legend, the reader is referred to web version of this article.)

with the wave number, without any significant variation. By contrast, Raman emissions measured from the pristine, non-confined compounds (see Fig. 7b–d: black lines) show a complex fluorescence/Raman spectra, composed by several bands characteristic of each molecular compound. In Fig. 7b–d, the same color line corresponding to the excitation geometries implemented in Fig. 7a has been assigned, thus Raman signals coming from the hybrid structures from the nanotube walls (green lines), from the porous cap layer (PCL: red lines) and from the opened barrier layers (OBLs: blue lines), can be easily identified. It is evident from Fig. 7a–d that the Raman signals detected for the pristine azo-dyes also dominate the emission spectra of the hybrid composites for all implemented experimental geometries: the high content and the absorptive properties of these LC azo-dyes overshadow the strong Raman emission of the AAM matrix (see Raman intensity scale in Fig. 7a for the PR-AAM), and the maximum emission peaks observed in Fig. 7b–d for the hybrid samples, in all three optical excitation geometries, correspond very well to the emission peaks of the pristine, non-confined molecules. These

results unambiguously demonstrate the abundant presence of the guest molecular structures inside the membrane nanotubes (green lines) and on their respective layers (OBL: blue lines and PCL: red lines). As mentioned before, due to the highly absorptive characteristics of the studied LC azo-dyes (see Fig. 6), the stronger Raman emission of the PR-AAM is fully absorbed by the guest molecules contained in the hybrid samples. This last fact, in combination with the similar Raman emission intensities observed in the hybrid samples for all implemented experimental geometries, which are in the same order of magnitude as that observed for the pristine, non-confined molecule, suggest a high LC molecular content inside the AAM nanotubes.

Finally, an SHG test was performed on the hybrid systems in order to investigate the quadratic NLO performance of such geometric nanoarrays, and most importantly, the molecular ordering of LC compounds achieved inside AAM. In fact, measurable SHG signals were detected for two of the hybrid samples, indicating an anomalous and stimulated ordering of the guest molecules induced by the nanotube walls during

drying. Fig. 8 shows the estimated NLO $\chi_{eff}^{(2)}$ macroscopic susceptibility coefficients evaluated according to the *Maker*-Fringes method for both the PR-AAM and the hybrid samples (an estimated experimental error of about 15% is considered). SHG measurements were performed implementing P-In/P-Out and S-In/P-Out laser beam polarization geometries. Since it is generally accepted that the walls of the pores are conformed by an amorphous centrosymmetric structure, formed by the aggregation of nanoparticles with sizes ranging from 2.5 to 4 nm and conformed by tetra and hexacoordinated aluminum (AlO_4 and AlO_6 polyhedral units) [57,58], the SHG produced by the PR-AAM is basically negligible (see Fig. 8). Only very weak surface SHG effects (generally detected by Lock-In amplification) may arise due to the symmetry breakdown typical of surfaces and interfaces or according to the quadrupole-moment mechanism [59,60]. This amorphous structure has been verified in our samples by X-ray diffraction (XRD) measurements (not shown here, see Ref. [50]) where a broad XRD spectra have been observed. By contrast, non-negligible SHG signals can be obtained from the hybrid structures, where

highest $\chi_{eff}^{(2)}$ coefficients were evaluated for the P-In/P-Out polarization geometry as: $\chi_{eff}^{(2)} \approx 0.25$ pm/V (RED-PEGM-7 hybrid), $\chi_{eff}^{(2)} \approx 0.08$ pm/V (RED-Me hybrid) and $\chi_{eff}^{(2)} = 0.0$ pm/V (RED-DIPEGM hybrid) (see Fig. 8a). The angle dependent SHG measurements (see Fig. 8b) do not exhibit any significant oscillating behavior (usual for non-phase matched Maker-Fringes experiments); this is due partially to the strong absorptive media at the SHG wavelength. For these reasons only the average effective $\chi_{eff}^{(2)}$ parameters were evaluated by direct comparison to the reference quartz sample and according to Eq. (1):

$$\chi_{eff}^{(2)\text{-hybrid}} \propto \chi_{11}^{(2)\text{-quartz}} \left(\frac{2l_c^{quartz}}{\pi l^{membrane}} \right) \left[\frac{I_{2\omega}^{hybrid}}{I_{2\omega}^{\chi_{11}^{(2)}\text{-quartz}}} \right]^{1/2}, \qquad (1)$$

where l_c^{quartz} is the coherence length of the quartz crystal (≈ 22 µm), $l^{membrane}$ is the AAM thickness and $I_{2\omega}^{\chi_{11}^{(2)}\text{-quartz}}$ is the SHG intensity at maximum of the *Maker*-Fringes observed for the reference crystal.

As expected, and according to Fig. 6, the weaker absorption spectra exhibited by the RED-PEGM-7 based hybrid allowed better conditions for SHG, obtaining for this system the highest $\chi_{eff}^{(2)}$ value. We argue that the occurrence of measurable SHG for the RED-PEGM-7 and RED-Me hybrids strongly suggests an average non-centrosymmetric molecular arrangement, evidenced by the angle dependent P-In/P-Out SHG measurements. This non-centrosymmetric arrangement may be caused in principle by the molecular interaction of the supported molecules on the nanotube walls during drying according to the XPS measurements and to the formation of convenient molecular aggregates (see below). However, since high absorption is observed in these structures, cascading NLO processes arising from cubic $\chi^{(3)}$ non-linearities may also contribute and should not be ignored [44–46]. In the case of the RED-DIPEGM hybrid, the observed saturated absorption spectra limit possible SHG. Besides, the highest molecular concentration of this non-diluted compound represents also a limitation for the NLO response due to the intermolecular dipole–dipole interactions caused by strong molecular aggregation, which according to the discussion of Section 3.3, should be of the anti-parallel H-type. In the case of the RED-PEGM-7 and RED-Me based hybrids, the observation of SHG signals suggests the formation of head-to-tail J-type aggregates.

4. Conclusions

The mechanically induced insertion of LC azobenzene dyes into the nanotube arrays of prepared oxalic AAM was monitored by AFM, absorption and Raman/fluorescence spectroscopies, and by the NLO-SHG technique. The chemical interaction of these molecular systems with the AAM–host matrix was investigated by XPS. According to the strong emissions detected by means of the fluorescence measurements (performed inside the nanotube cross-sections), high azo-dye content is confirmed within the host AAM nanotubes. XPS measurements demonstrated, through the Al 2p binding
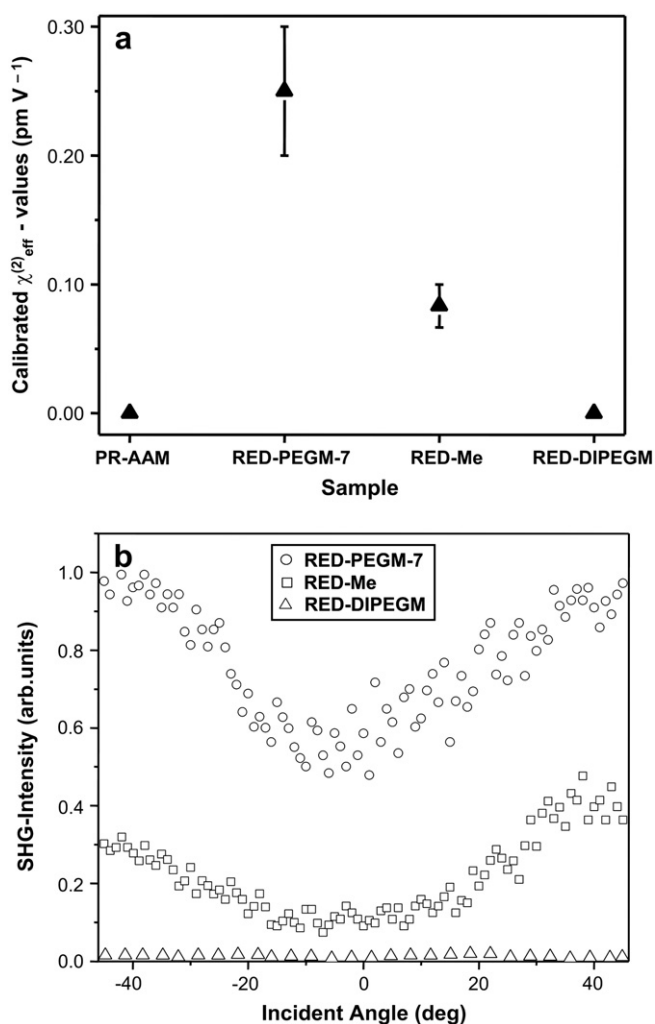

Fig. 8. NLO measurements performed on the AAM-hybrid composites according to the SHG Maker-Fringes technique: (a) calibrated $\chi_{eff}^{(2)}$ NLO-coefficients and (b) angle dependent SHG measurements (P-In/P-Out geometry).

energy, stronger atomic binding for RED-PEGM-7 compound, a weaker chemical interaction for the RED-DIPEGM molecule and only a mechanical interaction for the RED-Me molecular system. Although RED-DIPEGM possesses the higher dipole moment among the studied dyes, due to strong molecular aggregation, no SHG was observed for the respective hybrid, whereas non-negligible SHG signals were measured for the RED-Me and RED-PEGM-7 composites. The lower absorption observed for the RED-PEGM-7 based hybrid, and probably the stronger chemical binding of this compound with AAM, has enabled it to exhibit highest quadratic NLO coefficient ($\chi_{\text{eff}}^{(2)} \approx 0.25$ pm/V), which was estimated according to the relative Maker-Fringes calibration method. This compound has been previously studied in sonogel based hybrid systems [61] and shows an improved NLO performance within the AAM environment. Nevertheless, additional investigations should be performed in order to further understand the role played by the AAM nanotubes in the fabrication of the studied hybrid systems for optical applications, as well as their orientation and symmetry properties.

According to AFM, SHG and Raman studies, moderate but non-negligible molecular inclusion was achieved for the implemented compounds by convenient THF:dopant dissolutions. TEM and gravimetric measurements will be necessary in order to further clarify this point and quantify the amount of molecules inserted inside AAM. The RED-DIPEGM structure was poorly introduced in its natural LC state (at same vacuum conditions and room temperature), which may be related to its intrinsic high viscosity. Since all studied LC azo-dyes show thermotropic mesogenic behavior [30,31,61], the thermal insertion process should also be investigated in order to find the most favorable conditions for optimal incorporation of the studied molecular structures; in such case, it is expected that LC or even the isotropic mesophases, can be optimally inserted within the AAM nanotubes by capillarity and diffusion processes. Such experiments are currently underway.

Acknowledgements

References

[1] Diggle JW, Downie, Goulding CW. Chem Rev 1969;69:365−99.

[2] Thompson GE, Furneaux RC, Wood GC, Richardson JA, Goode JS. Nature 1978;272:433−5.

[3] Martin CR. Science 1994;266:1961−6.

[4] Rutkevitch D, Tager AA, Haruyama J, Almawlawi D, Moskovits M, Xu JM. IEEE Trans Electron Devices 1996;43(10):1646−58.

[5] Li AP, Müller F, Birner A, Nielsch K, Gösele U. J Appl Phys 1998;84(11):6023−6.

[6] Nielsch K, Choi J, Schwirn K, Wehrspohn RB, Gösele U. Nano Lett 2000;2(7):677−80.

[7] Lajos G. Characterization and optical theory of nanometal/porous alumina composite membranes. Ph.D. thesis, The University of Colorado, Colorado, USA; 1997.

[8] Xu TT, Piner RD, Ruoff RS. Langmuir 2003;19:1443−5.

[9] Sui YC, González JA, Bermúdez A, Acosta D, Feuchtwanger RJ, Flores JO, et al. Mater Res Soc Symp Proc 2001;633:A13.51.1−8.

[10] Zhang XY, Zhang LD, Li GH, Zhao LX. Mater Sci Eng 2001;A308:9−12.

[11] Iwasaki T, Motoi T, Den T. Appl Phys Lett 1999;75(14):2044−6.

[12] Paulus PM, Luis E, Kröll M, Schmid G, Jongh LJ. J Magn Magn Mater 2001;224:180−96.

[13] Lei Y, Liang CH, Wu YC, Zhang LD, Mao YQ. J Vac Sci Technol 2001;B19(4):1109−14.

[14] Shi G, Mo CM, Cai WL, Zhang LD. Solid State Commun 2000;115:253−6.

[15] Zhou Y, Shen C, Li H. Solid State Ionics 2002;146:81−6.

[16] Klein JD, Herrick RD, Palmer D, Sailor MJ, Brumlik CJ, Martin CR. Chem Mater 1993;5:902−4.

[17] Sui YC, González-León JA, Bermúdez A, Saniger JM. Carbon 2001;39:1709−15.

[18] Sui YC, Acosta DR, González JA, Bermúdez A, Feuchtwanger J, Cui BZ, et al. J Phys Chem B 2001;105:1523−7.

[19] Fuertes AB. Carbon 2002;40:1597−617.

[20] Varghese OK, Gong D, Dreschel WR, Gong K, Grimes CA. Sens Actuators 2003;B94:27−35.

[21] Fujiwara Y, Amao Y. Sens Actuators 2003;B89:187−91.

[22] Yamamoto Y, Baba N. Thin Solid Films 1983;101:329−38.

[23] Fukuda Y, Fukushima T. Bull Chem Soc Jpn 1980;53:3125−30.

[24] Ozao R, Ochiai M, Ichimura N, Takahashy H, Inada T. Thermochim Acta 2000;352/353:91−7.

[25] Mardilovich PP, Govyadinov AN, Mukhurov NI, Rzhevskii AM, Paterson R. J Membr Sci 1995;98:131−42.

[26] Thompson GE, Wood GC. Nature 1981;290:230−2.

[27] Rabek JK, editor. Photochemistry and photophysics, vol. 2. Boca Raton, FL: CRC Press; 1990. p. 119.

[28] Yesodha SK, Pillai CKS, Tsutsumi N. Prog Polym Sci 2004;29: 45−74.

[29] Natansohn A, Rochon P. Chem Rev 2002;102(11):4139−75.

[30] Rivera E, Belletête M, Natansohn A, Durocher. Can J Chem 2003;81:1076−82.

[31] Rivera E, Carreón-Castro MP, Buendía I, Cedillo G. Dyes Pigments 2006;68:217−26.

[32] Rivera E, Carreón-Castro MP, Rodriguez L, Cedillo G, Fomine S, Morales-Saavedra OG. Dyes Pigments 2007;74:396−403.

[33] He XH, Zhang HL, Yan DL, Wang X. J Polym Sci Part A Polym Chem 2003;41:2854−64.

[34] Tian YQ, Watanabe K, Kong XX, Abe J, Iyoda T. J Polym Sci Part A Polym Chem 2002;14:2197−206.

[35] Saito M, Shimomura T, Okumura Y, Ito K, Hayakawa R. J Chem Phys 2001;114:1−3.

[36] Shimomura T, Funaki T, Ito K, Choi BK, Hashizume T. J Inclusion Phenom Macrocycl Chem 2002;44:275−8.

[37] Takashima Y, Nakayama T, Miyauchi M, Kawaguchi Y. Chem Lett 2004;33:890−1.

[38] Ikeda T, Ooya T, Yui N. Regulation of pseudo-polyrotaxane formation between α-cyclodextrins and azobenzene-terminated poly(ethylene glycol). Polym J 1999;31:658−63.

[39] Tung CH, Wu LZ, Zhang LP. Acc Chem Res 2003;36(1):39−47.

[40] Samson AJ, Kenneth J, editors. ACS symposium series, vol. 672; 1995.

[41] Prasad PN, Williams DJ. NLO effects in molecules and polymers. Wiley; 1991. p. 3−7.

[42] Rao CNR, editor. Chemistry of advanced materials. Oxford: Blackwell Scientific Publications, CRC Press; 1993.

[43] Lindsay GA, Singer KD, editors. Polymers for second nonlinear optics. ACS symposium series no. 601. Washington, DC; 1995.

[44] Nalwa HS, Miyata S, editors. Nonlinear optics of organic molecules. CRS Press Inc.; 1997.

[45] Kajzar F, Swalen JD, editors. Organic thin films for waveguiding nonlinear optics. San Jose: Gordon and Breach Publishers; 1996.

[46] Marder SR, Sohn JE, Stucky GD. Materials for nonlinear optics, chemical perspectives. In: ACS symposium series, vol. 455. Washington, DC: American Chemical Society; 1991.

[47] Tredgold RH. J Mater Chem 1995;5:1095−106.

[48] Hall RA, Hara M, Knoll W. Langmuir 1996;12(10):2551−5.

[49] Lupo D, Ringsdorf H, Schuster A, Seitz M. J Am Chem Soc 1994;116(23):10498−506.

[50] Mata-Zamora ME, Saniger JM. Rev Mex Fis 2005;51(5):502−9.

[51] Li AP, Müller F, Birner A, Nielsch K, Gösele U. J Vac Sci Technol 1999;A17(4):1428−31.

[52] Beamson G, Briggs D. High resolution XPS of organic polymers. UK: John Wiley & Sons; 1992. p. 1−45.

[53] SDP v4.1 (32 bit) Copyright© 2004, XPS International, LLC, Compiled; January 17, 2004.

[54] Boyd RW. Nonlinear optics. Academic Press; 1992. p. 65−7.

[55] Ma X, Zhang H, Xu J. Chem Phys Lett 2002;363:579−82.

[56] Zhou Y, Shen C, Huang J, Li H. Mater Sci Eng 2002;B95:77−82.

[57] Partermarakis G, Moussoutzanis K, Chandrinos J. Appl Catal A Gen 1999;180:345−58.

[58] Farnan I, Dupree R, Jeong Y, Thompson GE, Wood GC, Forty AJ. Thin Solid Films 1989;173:209−15.

[59] Zhong-Can OY, Yu-Zhang X. Phys Rev 1985;A32:1189−200.

[60] Shtykov NM, Barnik MI, Beresnev LA, Blinov LM. Mol Cryst Liq Cryst 1985;124:379−90.

[61] Morales-Saavedra OG, Castañeda R, Villagran-Muniz M, Flores-Flores JO, Bañuelos JG, Saniger JM, et al. Mol Cryst Liq Cryst 2006;449:161−77.